Acta Materialia 306 (2026) 121875

Contents lists available at ScienceDirect

Acta Materialia

journal homepage: www.elsevier.com/locate/actamat

High-temperature phase transformation mechanisms in the U-2.5Mo-2.5Ti-5.0Zr (U-MT5Z) quaternary alloy

Wangwei Ru [a], Kun Yang [a,b,*], Weiqian Zhuo [c], Mingliang Kang [d], Danwen Qin [d,**], Yibo Wang [a], Xiaobin Tang [a,b,*]

[a] Department of Nuclear Science and Technology, Nanjing University of Aeronautics and Astronautics (NUAA), Nanjing 211106, China
[b] Key Laboratory of Advanced Nuclear Technology and Radiation Protection, Ministry of Industry and Information Technology, Nanjing 211106, China
[c] National key laboratory of nuclear reactor technology, Nuclear Power Institute of China, Chengdu 610213, China
[d] Sino-French Institute of Nuclear Engineering and Technology, Sun Yat-sen University, Zhuhai 519082, China

ARTICLE INFO

Keywords:
Metallic fuel
Phase transformation mechanism
Ab initio molecular dynamics
Element migration

ABSTRACT

Metallic fuels are considered ideal candidates for fast reactors due to their excellent neutron economy, manufacturability, and high burnup potential. To date, the development of metallic fuels has been restricted by their relatively low structural and phase stability. The current research focuses on the high-temperature behavior of the quaternary metallic fuel (U-2.5Mo-2.5Ti-5.0Zr) by fundamentally understanding the thermally driven elemental and microstructural evolution using multiscale advanced material characterization techniques and first-principles calculations. Experimental results reveal that the addition of Ti and Mo significantly broadens the thermal stability range of the high-temperature γ-U phase, suppressing its thermal decomposition during thermal cycling. Furthermore, both DFT calculations and experimental results indicate that the formation of a Zr-Ti compound effectively retards zirconium migration, thereby improving microstructural stability under high-temperature scenarios. This research reveals the mechanisms of phase transformations and the microstructural evolution of quaternary uranium-based metallic fuels at the atomic scale, thereby advancing the theoretical foundation for fuel design and performance optimization in advanced fast-reactor fuel systems.

1. Introduction

The sodium-cooled fast reactors (SFRs) are among the most rapidly developed Generation IV reactor designs, closely aligning with commercial nuclear power plant requirements and demonstrating advantages such as high power density and enhanced safety features [1]. Typical fuel candidates for SFRs include metallic fuels and ceramic fuels. Compared to ceramic fuels, metallic fuels exhibit superior physical compatibility due to their hard neutron spectrum, ease of manufacturability, high burnup capability, and compatibility with pyro-processing [2]. Metallic fuels have been widely studied in the U.S. and U.K [3]. During the 1980s, the U.S. Integral Fast Reactor (IFR) program conducted extensive irradiation testing of U-10Zr fuel in the EBR-II reactor, demonstrating satisfactory performance with burnups of up to 10 % FIMA (fissions per initial metal atom) [4].

One key phenomenon observed in the U-10Zr fuel is constituent redistribution [5,6]. The constituent redistribution refers to Zr redistribution, driven by phase segregation in the fuel due to a temperature gradient, intense neutron irradiation, and differences in Zr solubility across phases [7]. (In this study, we use “Zr redistribution” to describe macroscopic or mesoscopic changes in the Zr concentration profile across the fuel, driven by burnup evolution or temperature gradients, whereas “Zr diffusion” and “Zr migration” are reserved for the atomic-scale motion of Zr atoms.) Typically, a three-region morphology develops in U-10Zr fuel, distinguished by Zr content, with low Zr content observed in the intermediate region [8]. The elemental segregation would decrease the melting point of the fuel, according to the U-Zr phase diagram, and further reduce the safety margin of the metallic fuel [9].

In contrast to U-10Zr, the constituent redistribution can be eliminated by substituting Mo to form the U-10Mo alloy, as shown by recent irradiation tests [10]. Therefore, the U-10Mo alloy, which exhibits single-phase behavior regardless of temperature gradient, is desirable for metallic fuel. Despite the superior phase stability, potential intensive FCCIs occurred in U-10Mo, as demonstrated in DFR Mark-II and -III back

* Corresponding author at: Department of Nuclear Science and Technology, Nanjing University of Aeronautics and Astronautics (NUAA), Nanjing 211106, China.
** Corresponding author.
E-mail addresses: kun.yang@nuaa.edu.cn (K. Yang), qindw3@mail.sysu.edu.cn (D. Qin), tangxiaobin@nuaa.edu.cn (X. Tang).

https://doi.org/10.1016/j.actamat.2025.121875
Received 2 July 2025; Received in revised form 3 December 2025; Accepted 26 December 2025
Available online 27 December 2025

in the 1960s. Therefore, the potential FCCI in U-Mo fuels made it challenging to achieve burnups beyond 3 at.% due to an unacceptable decrease in the cladding thickness [11]. Recently, U-Mo-Zr-Ti quaternary alloys with a lower γ-phase onset temperature (by Mo) and a higher melting point (by Zr and Ti) than uranium were proposed based on evaluations of the binary phase diagrams between U and Mo/Zr/Ti [12,13]. Early investigations were performed on the U-5.0Mo-4.3Ti-0.7Zr (wt.%) alloy [14–16], with PIE results showing that constituent redistribution was not observed in this alloy. However, significant FCCI occurred during irradiation, primarily due to the low Zr content and high Mo content [14]. Later, Zhuo [17,18] investigated two quaternary alloys with higher Zr and lower Mo contents, i.e., 90.0U-2.5Mo-2.5Ti-5.0Zr (U-MT5Z) and 90.0U-1.5Mo-1.5Ti-7.0Zr (U-MT7Z), primarily focusing on out-of-pile properties, such as micron-scale microstructures and macro-scale phase evolution and solid-state phase transitions. Despite extensive research on U-Mo and U-Zr alloys that has revealed their high-temperature phase stability and element redistribution behavior, studies on the UMTZ quaternary system remain limited, especially regarding element redistribution under high-temperature conditions [19].

In this work, thermal cycling treatments were performed on U-MT5Z alloys using differential scanning calorimetry (DSC) to obtain samples at elevated temperatures from the phase change point to an ultra-high melting point (1400 °C). To the best of our knowledge, most studies on metallic fuels have focused on phenomenological observations of Zr redistribution and phase transformation in alloys, without explicitly addressing how Ti additions modify Zr migration at the atomic scale. In this work, the hypothesis that Ti suppresses Zr migration in the γ-U matrix was proposed and validated. The current study demonstrates that Ti effectively increases the migration barriers of Zr and significantly reduces its diffusion capability via experimental and first-principles calculations, thereby providing a precise microscopic mechanism for the Ti-induced suppression of Zr migration. Multi-scale microstructure and phase characterization techniques were employed to fundamentally understand the temperature-dependent microstructure evolution.

Furthermore, first-principles calculations were employed to explore the mechanism of element redistribution, providing atomic-scale insights into the suppressive effect of titanium on zirconium migration and redistribution. Compared with previous studies on U-Mo and U-Zr systems, this work supplements high-temperature phase transformation and high-resolution microstructural data for the U-MT5Z alloy and further elucidates the complex atomic interactions in multicomponent alloys. Moreover, the U–MT5Z alloy exhibits superior γ-phase thermal stability compared to the conventional U–10Zr alloy. This work provides crucial theoretical support for the design of advanced quaternary fuel systems.

2. Experimental details

2.1. Sample fabrication

Depleted uranium powder with 99.9 % purity provided by Sun Yat-sen University was used as the precursor material. Zr, Ti, and Mo powders with 99.5 % purity and an average particle size of 1 μm were purchased from Macklin Biochemical Co., Ltd. The precursor powders were wet ball-milled (MITR-YXQM-2 L, China) in an Argon atmosphere for 24 h, with ethanol acting as the reaction agent [20]. Subsequent dry ball milling under identical configuration parameters (24 h duration) was performed to homogenize the U-MT5Z powder mixture [21]. The ball milling was carried out in stainless steel vessels with five 8 mm tungsten carbide balls at 500 rpm, with intermittent 10-minute cooling pauses after every 30-minute milling cycle to mitigate thermal catch-up. The sintering of U-MT5Z alloy was carried out in an arc-melting furnace with a vacuum pressure of −4 MPa (DC1300, LUSOON METALL, China). High-purity argon gas (99.99 %) was introduced into the furnace after the vacuum step by adjusting the internal pressure to −0.05 MPa. The alloy ingot was then subjected to a series of remelting cycles, with a current of 290A used during the arc-melting. Specifically, the ingot was flipped and remelted 7 times, with each cycle lasting approximately 3 min. After the alloy had been uniformly melted, the furnace was turned off, and the ingot was cooled in 20 min. The final yield of the ingot reaches over 90 % (post-melting mass / total mass of raw materials before melting) [22,23].

The as-fabricated alloy was polished using 180-, 600-, 1000-, and 1500-grit SiC abrasive papers to remove surface oxide layers. Subsequently, polishing using polycrystalline diamond suspensions (0.25 μm). Polished samples were then transferred to a glovebox with controlled atmosphere by high-purity Argon (O_2/H_2O < 0.1 ppm), followed by cutting into small slices with dimensions (thickness ≤ 2 mm) and masses (< 100 mg) using a low-speed diamond saw (Shenyang Kejing SYJ-150, China). The entire preparation workflow maintained continuous inert gas shielding to minimize oxidation during mechanical processing.

2.2. Temperature-dependent DSC test

The phase transition behavior of the U-MT5Z alloys were further characterized by a TGA (Thermogravimetric Analysis) and DSC (Differential Scanning Calorimetry) (NETZSCH, DSC 500 Pegasus, German), with a heating rate of 10 °C/min and cooling rate of 30 °C/min under a high-purity argon atmosphere (≥99.999 %, flow rate 100 mL/min). Differential scanning calorimetry (DSC) experiments were conducted on four sectioned samples over temperature ranges from room temperature to 650 °C, 950 °C, 1100 °C, and 1400 °C, respectively. Two thermal cycles were performed on the alloys: the first to eliminate thermal stress, which was not recorded, and the second to generate representative measurement outcomes.

All DSC specimens were obtained from a single large button ingot; four pieces of essentially identical dimensions were sectioned from the same parent sample to minimize compositional and initial microstructural variability before thermal testing. The XRD profiles on these sample coupons confirm the consistency of phase and chemical composition throughout the four samples (Fig. S1).

2.3. Microstructure characterization

The microstructures of the sample before and after thermal treatment at different temperatures were further characterized by SEM-EDS (TESCAN LYRA3 GM, BRUKER XFlash 6130), XPS (Kratos Axis Ultra DLD spectrometer), and TEM-EDS (Thermo Fisher Spectra 300 s TEM, Super-X). X-ray photoelectron spectroscopy (XPS) was employed to analyze the nanoscale chemical composition of the U-MT5Z samples' very top surface, used to confirm the absence of uranium oxide formation (Fig. S2). A wide-scan survey was performed over the binding energy range of 0–1350 eV.

The sample lamellas post-temperature treatment was then prepared by Focused Ion Beam (FIB) using a Thermo Fisher Scios2 dual-beam FIB/SEM system for site-specific sample fabrication. The sample lamella was first coarsely thinned using a 30 kV Ga+ ion beam at 1 nA, followed by fine thinning at 30 keV and 50 pA as the thickness approached approximately 400 nm. Finally, a low-voltage cleaning step was conducted at 5 keV and 7.7 pA to minimize surface damage and obtain an electron-transparent region when the thickness was reduced to about 200 nm. The specific area for the sample preparation by FIB covered the region of different crystalline phases subjected to elevated temperatures from as-cast, 650 °C, 950 °C, and 1400 °C, which can be seen in the following Fig. 1. The prepared FIB sample lamella was transferred to the TEM chamber directly post the sample preparation to avoid surface oxidation. Microchemical analysis and electron diffraction pattern acquisition was conducted using the Thermo Fisher Talos F200S analytical system.

The bulk sample coupons post-thermal treatments were further characterized by XRD using a copper source for phase-structure

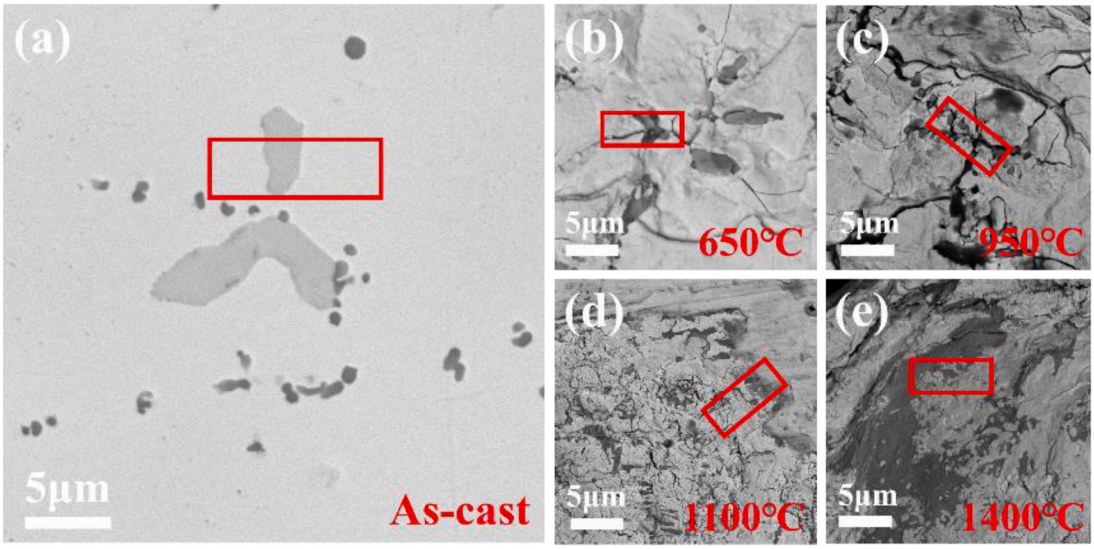

Fig. 1. FIB sampling regions. (a) The BSE micrographs of the sample before and after DSC treatment at (b) 650 °C, (c) 950 °C, (d) 1100 °C, and (e) 1400 °C. The red boxes indicate the regions selected for FIB sample preparation.

identification (PANalytical X'Pert Empyrean, Netherlands). The XRD instrument was calibrated with a silicon standard sample. In each XRD scan, the step size was 0.007162°/step, and the scan rate was 1°/min. The temperature-dependent phase transition behavior was further characterized by in situ X-ray diffraction (PANalytical Inc.) under an Argon atmosphere (150 ml/min). The diffraction patterns were collected over a 2θ range of 10°–90° with a scanning rate of 6°/min. The temperature was increased from 25 °C to 800 °C, with data recorded at 200 °C, 400 °C, 600 °C, and 800 °C. The heating rate was set to 2 °C/min, and the sample was held for 2 min at each temperature before data acquisition, enabling real-time monitoring of crystal structure evolution. In addition, the sample description and characterization techniques applied to each sample, together with brief notes on data quality and data availability, are provided in Table S1 of the Supplementary Material.

2.4. Ab-initio first-principles calculation

In this work, DFT calculations were performed using the projector-augmented wave method [22,23], as implemented in the Vienna Ab initio Simulation Package (VASP) [24,25]. The isolation of vacancy-adjacent Zr atoms dominates the rate-limiting steps of diffusion, and their migration barriers directly reflect the Zr redistribution degree [26].In particular, for the U-MT5Z system, the isolation of vacancy-adjacent Zr atoms excludes interference from alternative diffusion pathways and Mo atoms. However, previous studies [11,27,28] have shown that Mo inclusion primarily stabilizes the γ phase. Compared with conventional averaging approaches, this method provides deeper insight into the inhibitory mechanism of Ti-Zr interactions on atomic migration, enabling more sensitive detection of the intrinsic effects of alloyed Ti on Zr migration suppression [29].

The calculations were performed using the PerdewBurke–Ernzerhof (PBE) Generalized Gradient Approximation (GGA) density functional implementation for the description of the exchange-correlation [30,31]. Based on the convergence test results (Fig. S3), a Monkhorst-Pack [31,32] 5 × 5 × 5 k-point mesh was used for Brillouin zone sampling. Uranium is assumed to be non-magnetic, in accordance with experiments and previous simulations [26], and the energy cutoff was set to 350 eV. The electronic self-consistent loop convergence criterion is taken to be 10^{-6}. The PBE functional, supplemented with a Hubbard U, was applied to calculate the energetics using a plane-wave basis set and pseudopotentials, as implemented in the VASP program. Different Hubbard U values were applied for different systems. The Hubbard U parameters for the U-MT5Z system were calculated through using the linear response method [33], with a Hubbard U of 2.52 eV for uranium and 2.61 eV for zirconium, respectively (Fig. S4). For the U-10Zr system, the Hubbard U values were both 1.24 eV [34,35].

In this work, AIMD simulations were performed at 1100 °C, a temperature chosen for both physical relevance and computational feasibility. From the perspective of phase stability, thermal analysis and phase diagram data indicate that the U-MT5Z alloy preserved a γ-U phase at this temperature, consistent with our experimental observations, and that U–10Zr also adopts a γ-dominated structure in a similar temperature range, which enables a meaningful and directly comparable analysis of the atomic dynamics in both alloys. At the same time, AIMD is intrinsically limited to picosecond time scales; at substantially lower temperatures, atomic displacements become too small to adequately sample representative local rearrangements within a feasible simulation time. A temperature of 1100 °C provides sufficient thermal activation to reveal characteristic vibrational and relaxation behavior around defects, while remaining well below the melting regime, thereby offering a practical compromise between physical realism and computational efficiency. Alloy compositions within these values were generated by randomly substituting zirconium atoms for uranium atoms (or Ti/Mo atoms for uranium atoms) at lattice sites to simulate the 5 % and 10 % Zr substitutions for U-MT5Z and U-10Zr, respectively. The resulting atomic structures were verified using VESTA [36] to confirm the formation of random substitutional solid solution alloys.

The simulations were performed in the NVT ensemble using a Nose-Hoover thermostat for temperature control. A time step of 2.0 fs was employed, with 25,000 steps simulated for a total simulation time of 50 ps (Fig. S5). Before production runs, the system with the ideal structure was equilibrated for 5 ps using 1.0 fs time steps. All simulations were conducted on a 216-atom supercell (6 × 6 × 3 bcc unit cells) with periodic boundary conditions.

The bulk modulus is defined by Eq. (1):

$$B_0 = -V_0 \frac{\partial P}{\partial V} \tag{1}$$

Where B_0 is the bulk modulus, V_0 is the equilibrium total volume of the cell, and P and V are the pressure and volume, respectively [31]. The equilibrium lattice parameter is calculated from Eq. (2):

$$a = \sqrt[3]{\frac{V_0}{64}} \quad (2)$$

Where a is the equilibrium lattice parameter at temperature 1100 °C, the equilibrium total volume is divided by 64 (the total number of unit cells) to obtain the volume of the unit cell [31].

At elevated temperatures, the diffusion coefficients of different atomic species can be determined by calculating their mean squared displacements (MSD) under thermodynamic equilibrium conditions [37]. For individual atomic motion within the system, it should be noted that the trajectory is not a simple path. Continuous collisions with other atoms deflect the moving atom from its original trajectory during atomic migration. The MSD can be calculated by the following Eq. (3):

$$MSD = 6Dt + C \quad (3)$$

Where D represents the diffusion coefficient of migrating atoms, specifically referring to the Zr diffusion coefficients in γ-(U, Zr) and U-MT5Z alloys to be calculated, and C denotes the constant for initial displacement. Under elevated temperature conditions, MSD exhibits a linear relationship with time, with the slope bearing the following relationship to the atomic diffusion coefficient:

$$D = \lim_{t\to\infty}\frac{1}{6t}\left\langle |r(t) - r(0)|^2 \right\rangle \quad (4)$$

Where $r(t)$ and $r(0)$ represent atomic coordinates at time t and initial time, respectively [37–39].

According to the Einstein relation, the atomic diffusion coefficient exhibits a linear dependence on MSD over sufficiently long time scales, indicating that in atomic simulations, this relationship holds when the MSD-Δt curve demonstrates linear or quasi-linear behavior (where Δt denotes the time interval from the initial statistical moment) [37]. Under these conditions, the diffusion coefficient is the slope of this curve, independent of the time duration [40]. The diffusion coefficients can be determined by statistically analyzing the MSD during 5–50 ps in AIMD simulations. Subsequently, the high-temperature diffusion coefficients of Zr atoms in the γ-(U, Zr) and U-MT5Z systems were derived from the MSD-diffusion coefficient relationship [26,40].

In the AIMD simulations, a single U atom was deliberately removed from the same lattice site in both the γ-(U, Zr) and U-MT5Z models to construct a single-vacancy defect system, as previously demonstrated [41–43]. A root-mean-square displacement (RMSD) between the initial and relaxed atomic configurations was further calculated to quantify the thermal-driven local structural relaxation. The RMSD can be calculated by the following Eq. (5):

$$RMSD = \sqrt{\frac{1}{N}\sum_{i}^{natom}\left[\left(x_i - x_i'\right)^2 + \left(y_i - y_i'\right)^2 + \left(z_i - z_i'\right)^2\right]} \quad (5)$$

where N is the number of atoms considered, and $(x_i, y_i, z_i)$and (x_i', y_i', z_i')denote the Cartesian coordinates of atom i in the initial and relaxed structures, respectively.

3. Results

3.1. As-cast U-MT5Z

The XRD profiles and surface SEM images with corresponding EDS analysis for the as-cast U-MT5Z sample are shown in Fig. 2. The XRD result (Fig. 2a) indicates that the main phase of the alloy is γ-U, with no secondary phase. The SEM images (Fig. 2b and c) indicate three distinct contrast regions, i.e., bright, gray, and dark. The elemental mappings (Fig. 2d–g) suggest that U is uniformly distributed within the matrix, with scattered Zr precipitation observed. In addition, the precipitate size was further measured and found that the average size of the Zr precipitate in the as-cast sample is 1.76 μm², with most precipitates being smaller than 10 μm² (Fig. S6).

Fig. 3 presents the cross-sectional microstructure of the as-cast U-MT5Z sample prepared using focused ion beam (FIB) (corresponding to zone b in Fig. 1a) and characterized by STEM. As shown in Fig. 3a, the cross-sectional HADDF image reveals that nanosized precipitates are present in the matrix, with sizes of approximately 100–300 nm. The elemental mappings (Fig. 3b–e) indicate the distribution of various elements within the sample. The matrix is enriched in U, while the crystalline structure can be indexed as body-centered cubic (bcc) γ-U phase, along with weak α-U diffraction spots according to the SAED pattern (Fig. 3f). The nanosized precipitates enriched in Zr can be characterized as a hexagonal close-packed (hcp) structure (Fig. 3g). The result shows that the as-cast U-MT5Z sample exhibits a dual-phase structure composed of a γ-U matrix and hcp-Zr precipitates, with no significant segregation of Mo or Ti observed.

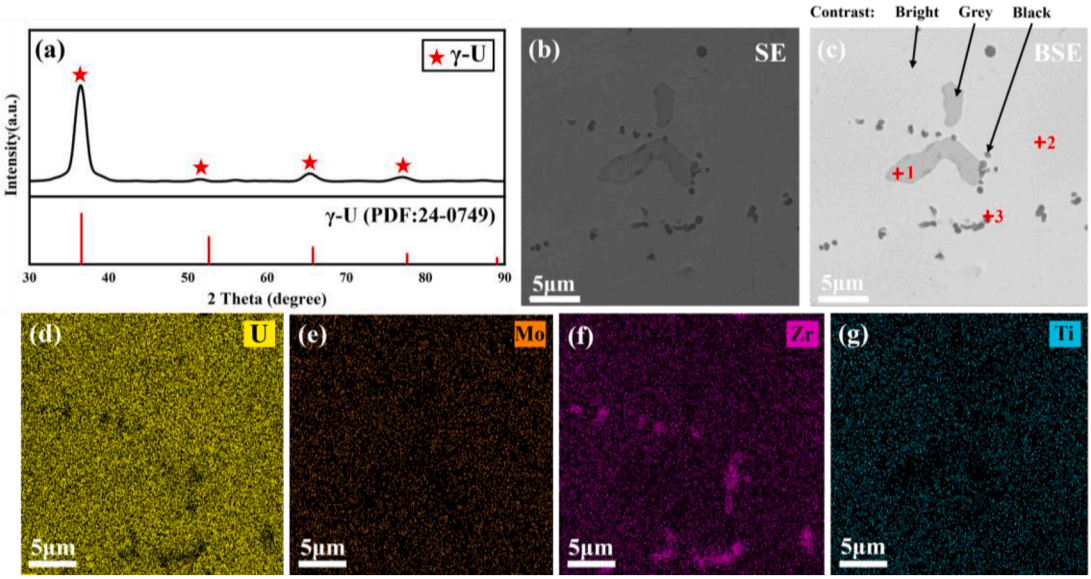

Fig. 2. Characterization results for as-cast U-MT5Z: (a) XRD. (b) SEM images with secondary electron (SE) mode, (c) SEM images with backscattered electron (BSE) mode, (e)-(h) Energy dispersive spectroscopy (EDS) elemental maps of (b). Note: EDS data are semi-quantitative and are used here to indicate relative compositional trends/enrichment rather than precise absolute compositions.

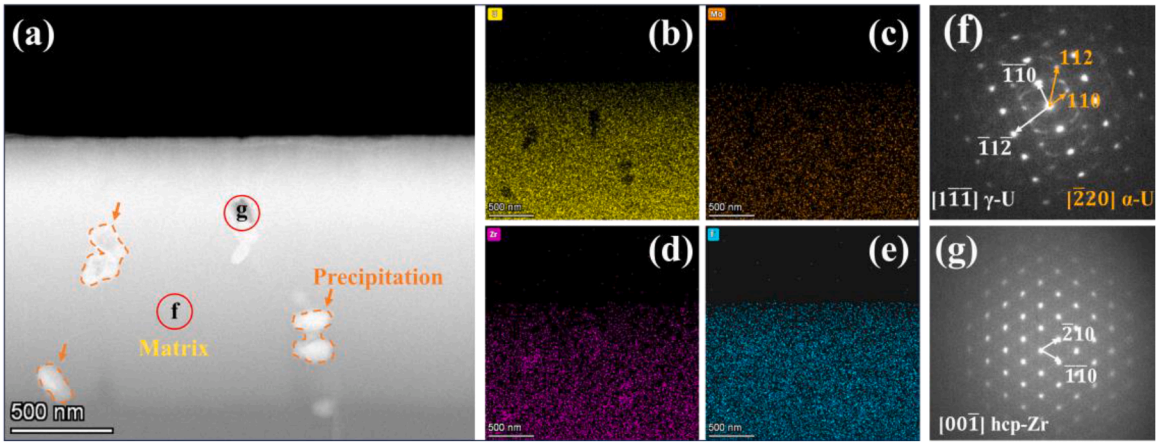

Fig. 3. TEM characterization of as-cast U-MT5Z sample. (a) High-angle annular dark-field (HAADF) image, (b)-(e) EDS elemental maps of (a), (f) Selected area electron diffraction (SAED) pattern of the matrix, (g) SAED pattern of the precipitate. Note: EDS data are semi-quantitative and are used here to indicate relative compositional trends/enrichment rather than precise absolute compositions.

3.2. Microstructure characterization of U-MT5Z after thermal treatments

3.2.1. Microstructure evolution of U-MT5Z after thermal treatment at 650 °C

The SEM and TEM results of the DSC-650 °C sample are shown in Fig. 4. The DSC-650 °C sample surface exhibits pronounced roughening and several microcracks (Fig. 4a-b). Distinct precipitates can be clearly identified on the surface in the BSE image (Fig. 4c), with Zr-rich precipitates identified by EDS analysis (Fig. 4d-h). The average size of the Zr precipitate (Fig. S6) shows a slight increase (4.21 μm^2) as compared to the as-cast sample (1.76 μm^2). TEM analysis was further conducted to verify the phase transformation behavior of the DSC-650 °C sample. According to TEM data (Fig. 4i–l), α-U and U_2Ti coexist in the sample. In the previous study on the U-MT5Z alloy, the α-*U* + *U*$_2$Ti → γ-U phase transformation during heating was reported [44], which suggests the γ-U → α-*U* + *U*$_2$Ti phase transition would take place upon cooling, vice versa. Moreover, the α-U and U_2Ti phases coexisted after the DSC treatment, further confirming that the γ-U → α-*U* + *U*$_2$Ti phase transformation occurred at the nano-scale [17,27,45].

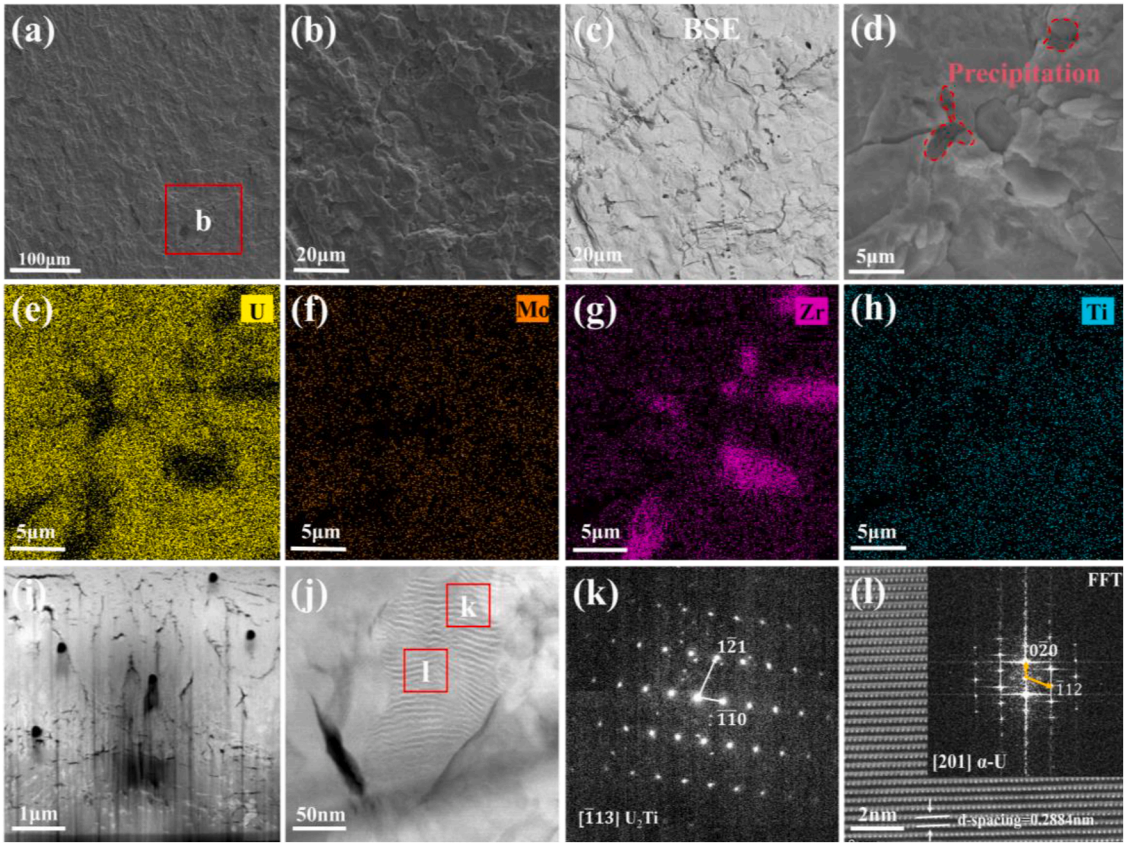

Fig. 4. SEM and TEM characterization of the DSC-650 °C sample. (a)-(d) Surface morphology, (e)-(h) EDS elemental maps of (d), (i) TEM image of U-MT5Z alloy, (j) high-resolution image of the matrix, (k) SAED pattern of the matrix, (l) atomistic images of the DSC-650 °C sample. Note: EDS data are semi-quantitative and are used here to indicate relative compositional trends/enrichment rather than precise absolute compositions.

3.2.2. Microstructure evolution of U-MT5Z after thermal treatment at 950 °C

The SEM images with corresponding EDS mappings for the DSC-950 °C sample are shown in Fig. 5. Compared to the sample after thermal treatment at 650 °C, dramatic surface spallation can be seen for the U-MT5Z sample post 950 °C thermal treatment, with a large number of cracks occurring (Fig. 5a-c). Phase segregation is observed along the cracking, while Zr was concentrated at the crack tips (Fig. 5d-g). Furthermore, Zr-Ti compounds were observed on the sample surface, consistent with the known preferential diffusion of Zr at high temperatures [46]. At this temperature, the average size of the Zr precipitate is 4.90 μm^2 (Fig. S6), showing no significant increase compared to the DSC-650 °C sample, but with a notable increase in the proportion of larger precipitates.

The HADDF image of the samples post 950 °C thermal treatment is shown in Fig. 6, with cracks and precipitation observed in the sample (Fig. 6a). The phase segregation, along with parallel-aligned lath-shaped precipitates, is observed at the sample bottom, approximately 10 μm from the top surface (Fig. 6a-e). The corresponding diffraction spots of the matrix according to the SAED (Fig. 6f) highly match those of γ-U, while suggesting the precipitates (Fig. 6g) are a bcc Zr-Ti structure.

3.2.3. Microstructure evolution of U-MT5Z after thermal treatment at 1100 °C

Compared to the sample after thermal treatment at 950 °C, the surface cracks gradually disappeared, evolving into elongated cracks in the DSC-1100 °C sample (Fig. 7a-b). In addition, the average size of the Zr precipitate in the DSC-1100 °C sample reached 7.81 μm^2, showing a significant increase compared to the previous three samples (As-cast, DSC-650 °C, DSC-950 °C). The proportion of smaller precipitates (<10μm^2) decreased, while the proportion of larger precipitates (>10 μm^2) notably increased (Fig. S6). Furthermore, severe surface spallation with a clear triple-layer structure can be observed in the DSC-1100 °C sample, as shown in Fig. 7c-g. Region I and Region III are primarily composed of U-Mo-Ti solid solution, while Region II is dominated by Zr-Ti precipitates (Fig. 7h). Therefore, the high-temperature thermal treatment led to phase separation and changes in the alloy's element distribution.

A distinct lath-shaped precipitates were observed about 7 μm below the top surface for the DSC-1100 °C sample, as compared to the sample after thermal treatment at 950 °C (Fig. 8a-e). Moreover, the γ-U phase can still be identified in the sample matrix after 1100 °C thermal treatment, with the precipitates featuring bcc Zr-Ti solid solutions (Fig. 8f and g). These results showed that no new phase transformations occur in the DSC-1100 °C sample during thermal cycling from 950 to 1100 °C, while the Zr-Ti solid solutions tend to migrate toward the sample surface.

3.2.4. Microstructure evolution of U-MT5Z after thermal treatment at 1400 °C

Compared to the samples treated at 950 °C and 1100 °C, the DSC-1400 °C sample exhibits a significant number of Zr-Ti precipitates on the surface (Fig. 9a and (a1) -(a4)). The average size increased to 11.95 μm^2, nearly 10 times that of the as-cast sample (Fig. S6). Furthermore, this sample also exhibits the highest proportion of large-scale precipitates (130 μm^2), confirming the thermodynamically driven growth of the precipitates. Large Zr-Ti precipitates featured with bcc structure can further be identified in the TEM analysis (Fig. 9b and (b1) -(b4)) with the matrix remaining γ-U phase after 1400 °C heat treatment according to the corresponding SAED results (Fig. 9c-d). The phase property of the bulk sample was further characterized by XRD (Fig. 9e), which clearly confirms that the main phase of the DSC-1400 °C sample is γ-U, and no secondary phases were detected. Therefore, the U-MT5Z alloy system can maintain the macroscopic stability of the γ-U phase structure even at 1400 °C.

4. Discussion

4.1. Temperature-dependent phase transition behavior of U-MT5Z

Although the phase transformation behavior of the U-MT5Z alloy has attracted increasing attention, the underlying mechanism governing the temperature-dependent phase transformation, as well as the microstructure evolution of U-MT5Z during phase transformation, remains

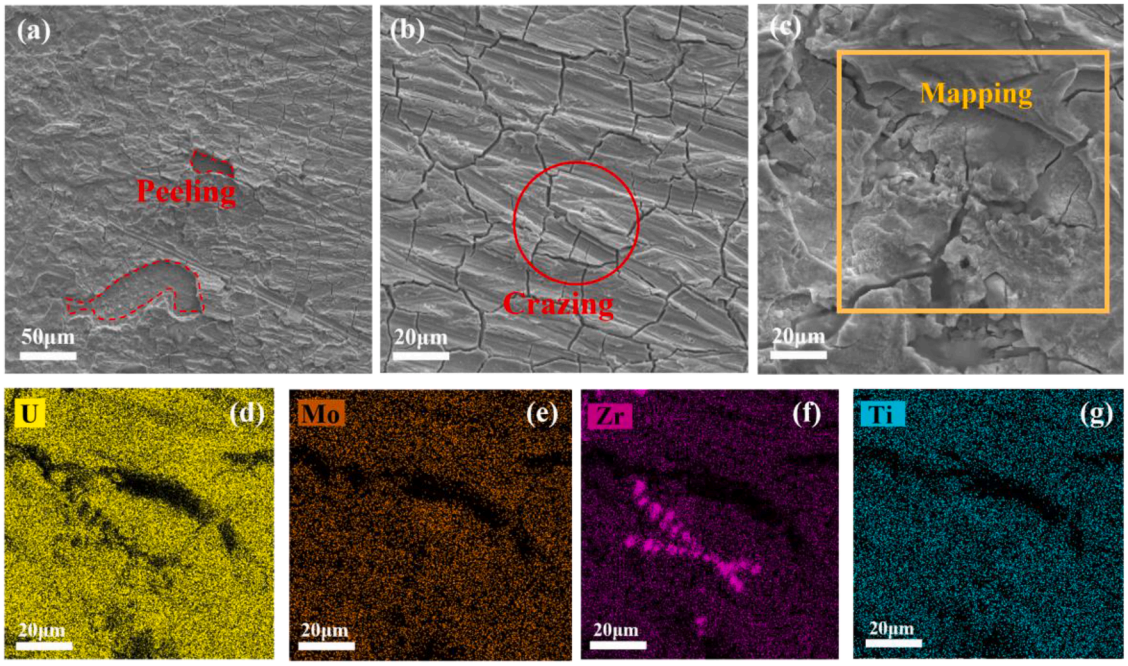

Fig. 5. Microstructure of the sample post thermal cycling treatment of 950 °C. (a)–(c) SEM images with SE mode and the selected EDS mapping regions marked in yellow, (d)–(g) EDS elemental maps for the rectangle region in (c). Note: EDS data are semi-quantitative and are used here to indicate relative compositional trends/enrichment rather than precise absolute compositions.

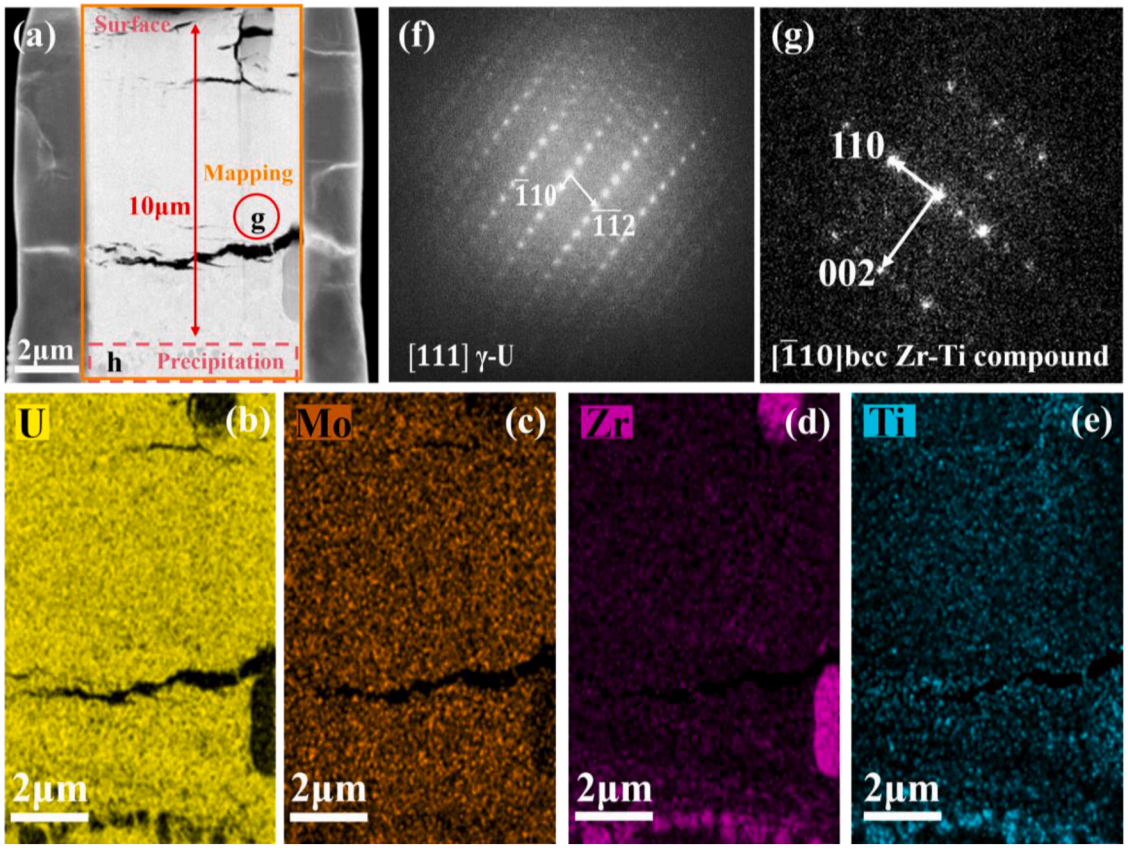

Fig. 6. (a) HAADF image of the DSC-950 °C sample, (b)–(e) EDS elemental maps for the rectangle region in (a), (f) SAED pattern of the matrix, (g) SAED pattern of the precipitate. Note: EDS data are semi-quantitative and are used here to indicate relative compositional trends/enrichment rather than precise absolute compositions.

unknown. Herein, the temperature-driven phase transformation is discussed, which further correlates with the redistribution of the constituents.

The intrinsic phase transformation behavior of the metallic fuel significantly limits its high burnup potential by readily driving phase transformation and further accelerating FCCI. Ensuring the thermal stability of metallic fuel by stabilizing its crystalline phase is critical for the long-term safe operation of nuclear reactors. The α-phase in uranium-based alloys, characterized by its anisotropic structure, is prone to pronounced thermal cycling-induced growth, leading to volume expansion and a porous structure that compromises the material's structural integrity. This growth effect of α-U is primarily attributed to the thermal ratcheting mechanism, in which the anisotropy of α-U leads to differential thermal expansion coefficients in different directions, causing relative displacement between adjacent grains, facilitating internal stress relaxation, and resulting in permanent structural modifications [47,48]. For comparison, the γ-phase U demonstrates exceptional thermal stability, with minimal grain growth during thermal treatment and a higher thermal conductivity [27,49]. Therefore, the γ-phase starting temperature and its thermal stability temperature window are critical for evaluating the performance of U-based alloys.

U-10Zr, as a predominant component in metallic fuels, offers many advantages. However, according to the phase diagram (Fig. S7a), U-10Zr underwent multiple phase transitions over similar temperature ranges, leading to element redistribution that significantly impacts the fuel's performance. In contrast, no compositional redistribution has been observed in U-10Mo. The U-10Mo alloy remains single-phase above 600 °C, ensuring it remains single-phase throughout the process, regardless of the temperature gradient. Furthermore, Mo is considered a stabilizer for the γ phase, lowering its starting temperature (e.g., pure uranium at 776 °C [50], U-10Zr around 680 °C [50], and U-10Mo at 555 °C [28]). A lower γ phase transition point allows the fuel to remain in a single γ phase over a broader high-temperature range or to have a larger proportion of γ phase. Moreover, with temperature fluctuations, the likelihood of phase transitions in the fuel decreases, thereby reducing instability caused by phase changes. Despite the superior phase stability, potential intensive FCCIs occurred in U-10Mo, as demonstrated in DFR Mark-II and -III back in the 1960s.

The DSC results of the U-MT5Z alloy are shown in Fig. 10. Three phase transition peaks were found in Fig. 10a. It is suggested that the first peak (Fig. 10b) corresponds to the α → γ phase transformation according to the STEM analysis and phase diagram in Fig. S7. The onset temperature of the γ phase is determined to be 609 °C for the U-MT5Z alloy, a result that aligns with previous studies by Zhuo et al. [44]. Specifically, similar starting temperatures for the γ-phase transformation across similar compositions and experimental conditions can be observed. The current research further validates the high-temperature phase transformation behavior of the U-MT5Z alloy, which shows similarities to other quaternary alloys (such as U-MT7Z) when compared with data from these studies [44]. Additionally, an interesting phenomenon was observed in this study: a trace amount of α-U phase was detected in the DSC at 650 °C, which can be attributed to temperature gradients and differences in alloy composition [51] (Fig. 4l). The high-temperature stable γ-U phase transforms into the α-U phase as the temperature decreases, which is stable at lower temperatures during the cooling process. The transformation between the γ-U and α-U phases is a common phenomenon in U-based alloys, particularly during the cooling process [52]. This process may be promoted by internal stresses, cooling rates, and differences in the distribution of elements within the alloy. Aizenshtein et al. [53] also observed a similar

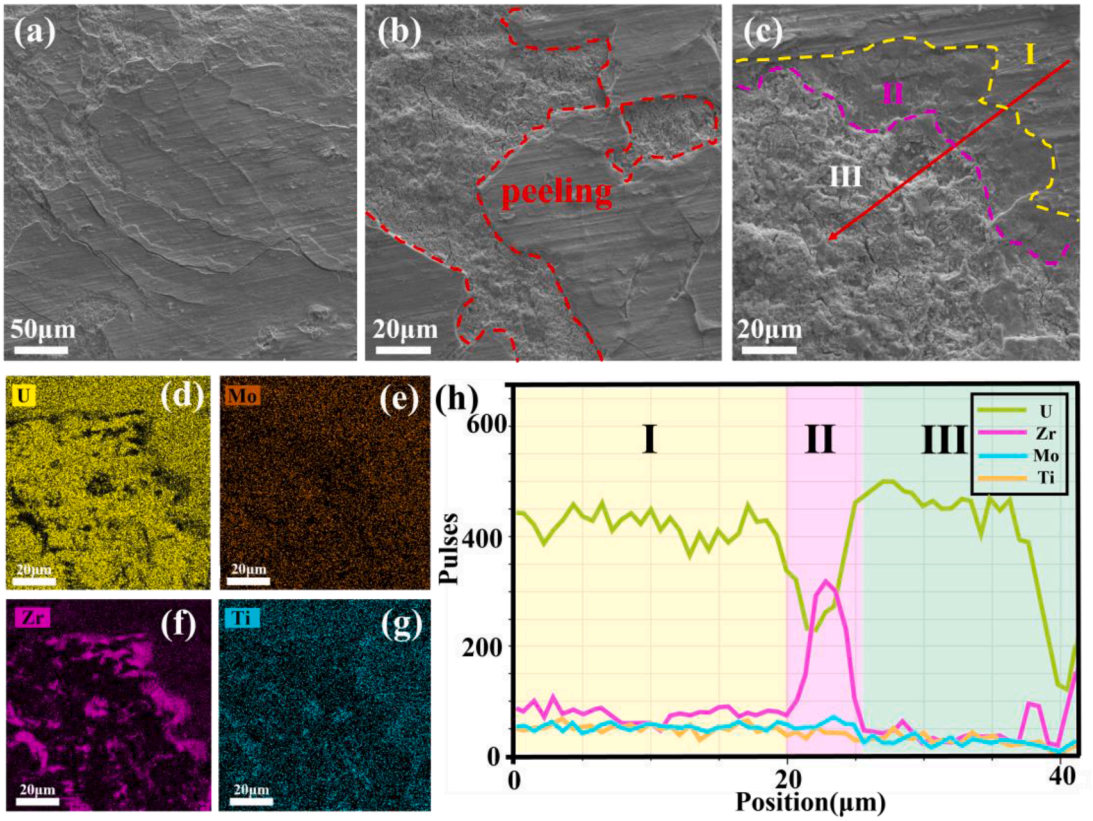

Fig. 7. Microstructure of the sample post thermal cycling treatment of 1100 °C. (a)–(c) Surface morphology, (d)–(g) EDS elemental maps of (c), (h) EDS line scan along the red line in (c). Note: EDS data are semi-quantitative and are used here to indicate relative compositional trends/enrichment rather than precise absolute compositions.

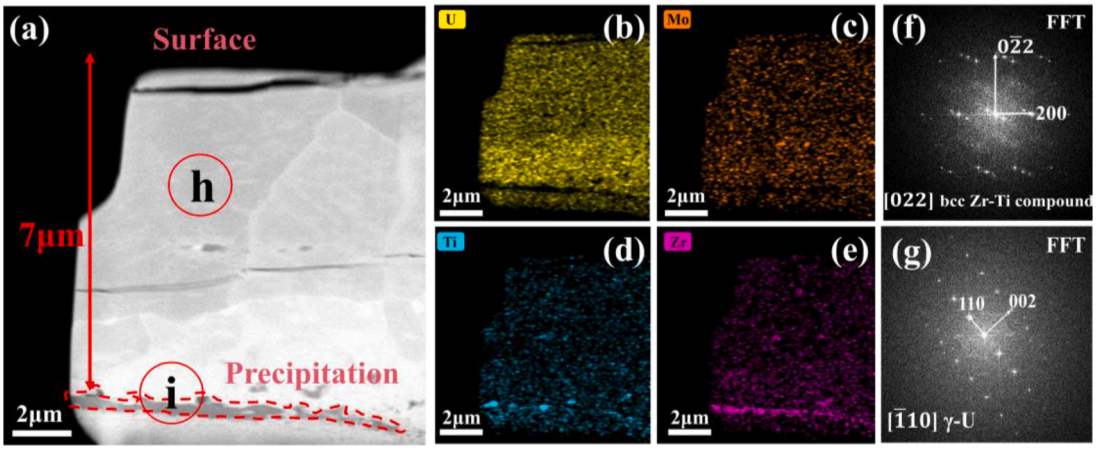

Fig. 8. (a) HAADF image of the DSC-1100 °C sample, (b)–(e) EDS elemental maps of (a), (f) SAED pattern of the matrix, (g) SAED pattern of the precipitate. Note: EDS data are semi-quantitative and are used here to indicate relative compositional trends/enrichment rather than precise absolute compositions.

phase transformation in their study of U-Ga alloys, suggesting that the γ-U phase readily transforms into the α-U phase, and that this transformation typically exhibits delayed kinetics and distinct kinetic features due to differences in cooling rates during thermal treatment. Therefore, the DSC tests were conducted on a single sample at different cooling rates (5, 10, and 15 °C/min). Results clearly denoted that the cooling rates have a slight influence on the peak position, further demonstrating that the observed phase transitions are thermodynamically driven rather than strongly dependent on cooling kinetics (Fig. S8).

The incorporation of Mo and Ti further broadens the thermal stability window as compared to U-10Zr alloys. The γ phase transformation occurs at approximately 680 °C in the U-10Zr alloy, which is significantly higher than the transformation temperature observed in this study (609 °C), suggesting that the U-MT5Z alloy plays a significant role in lowering the starting temperature of the γ phase [44]. Moreover, the γ-U in U-MT5Z alloy demonstrates higher phase stability without manifest secondary phase detected at 1400 °C as evidenced by the XRD analysis in Fig. 9e. A second phase transition peak was observed in the DSC results at 950 °C, 1100 °C, and 1400 °C, which corresponds to a secondary phase transformation within the U-MT5Z alloy, i.e., the U_2Ti → γ phase transition (Fig. 10c, Fig. 4k and Fig. S7b).The third peak (Fig. 10d) corresponds to the melting point of the U-MT5Z alloy, which

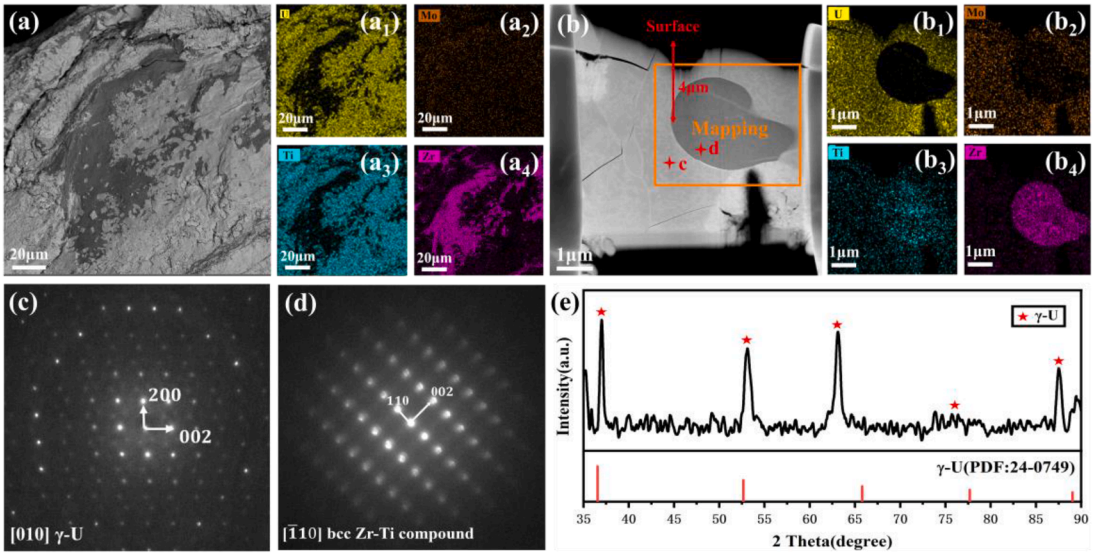

Fig. 9. Characterization results of the DSC-1400 °C sample. (a) SEM image and EDS elemental maps, (b) HAADF image of the yellow box in (a) and EDS elemental maps of the rectangle region in (b), (c) SAED pattern of the matrix, (d) SAED pattern of the precipitate, (e) XRD profile for the sample coupon. Note: EDS data are semi-quantitative and are used here to indicate relative compositional trends/enrichment rather than precise absolute compositions.

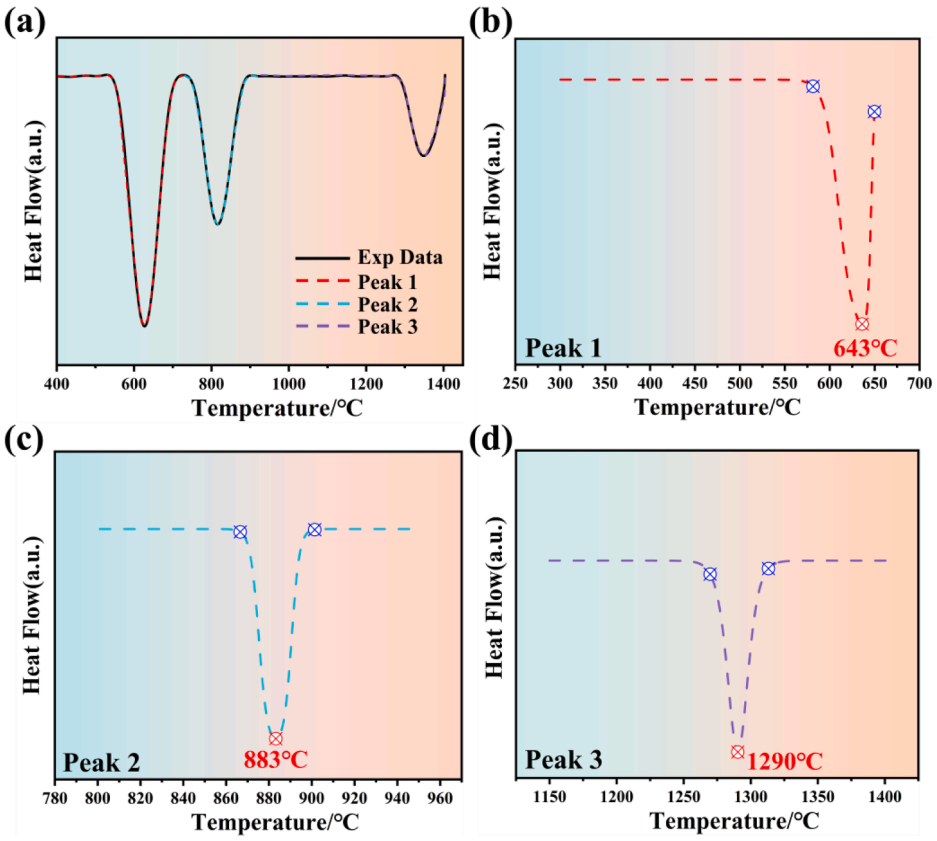

Fig. 10. Binary phase diagrams of U-Zr and U-Ti systems and DSC results of U-MT5Z alloy. (a) DSC result of U-MT5Z alloy after thermal cycling at 1400 °C, (b) peak fitting, peak 1, (c) peak 2, (d) peak 3.

is approximately 6 % higher than the U-10Zr alloy. Therefore, compared to the traditional U-10Zr alloy, the U-MT5Z alloy shows a significant reduction in the γ-phase starting temperature, approximately 9 % lower than that of U-10Zr, and a 13 % higher γ-U stability temperature than the binary U-10Zr, indicating an expansion of the thermal stability window. The in-situ XRD results (Figs. S9–10) further confirmed this conclusion, showing crystal structure evolution consistent with expectations. The in-situ XRD patterns reveal the phase transformation of U-alloys with increasing temperature. At 200 °C, the alloy primarily consists of the α-U phase (43.8 %), with minor contributions from γ-U (16.1 %). As the temperature increases to 400 °C and 600 °C, the α-U phase persists, while the γ-U phase fraction begins to increase. At 800 °C, the γ-U phase becomes dominant (85.92 %), while the α-U (0.044 %) and U_2Ti phases (14.034 %) significantly reduce. Overall, these results

suggest that, compared to traditional U-10Zr and U-Mo alloys, the U-MT5Z alloy not only exhibits a wider stable temperature range for the γ-U phase but also demonstrates exceptional thermal stability, significantly enhancing its potential for applications in high-temperature environments.

4.2. Thermal-driven Zr migration in U-MT5Z alloy

The constituent redistribution is another important factor affecting the performance of uranium-based alloys. The constituent redistribution in the U-10Zr alloy occurred rapidly and was completed at approximately 5 at. burnup. %, leads to the composition discrepancy across the radial direction [54]. Specifically, three distinct regions, based on Zr content, can be classified into central, intermediate, and peripheral regions [8]. The Zr-enrichment is higher in the central region, while it is lower in the intermediate region, and approximately equal to the nominal composition in the peripheral region [55–57]. The prevailing explanation for elemental redistribution is that high temperatures and thermal gradients are the primary driving forces, with irradiation further intensifying the effect [57–59]. The temperature within the fuel decreases progressively from the center to the periphery, leading to the formation of the γ phase in the center and an intermediate region dominated by a β+γ phase. The peripheral region predominantly contains the α phase, with low Zr solubility, consistent with the current study [60–64].

The current study found that Zr element redistribution also occurred in the U-MT5Z alloy, with significant Zr segregation at the crack sites (Fig. 4c and Fig. 5c). Specifically, banded precipitates featuring a Zr-Ti solid solution of the U-MT5Z alloy after thermal treatment at 950 °C were located about 10 μm from the sample surface. However, a similar lamella phase segregation structure was also observed at about 7 μm from the surface in the sample after thermal treatment at 1100 °C, suggesting that the gradual migration of the secondary phase towards the top surface is thermodynamically driven (Fig. 8a-e). This is consistent with the common behavior of Zr in U-based alloys (Aizenshtein et al. [65]), where at high temperatures Zr typically migrates to cooler regions (the peripheral region), causing phase separation [66]. Besides, the Ti element effectively suppresses excessive migration of Zr within the alloy by forming a Zr-Ti solid solution, as denoted in the current study, rather than the widespread Zr-rich phase observed in U-10Zr alloys [67].

The potential impact of Ti or the Zr-Ti solid solution on the delay of Zr migration can be attributed to the strong tendency of the Zr-Ti binary alloy system to form continuous solid solutions across the entire compositional range due to their similar hexagonal close-packed (hcp) crystal structures and a minor atomic size mismatch ($\Delta r \approx 4.3$ %), which can be detailed in the schematic Fig. 11 [68–70]. Specifically, the lattice parameters of Zr are $a = 0.323$ nm and $c = 0.514$ nm, while those of Ti are $a = 0.295$ nm and $c = 0.468$ nm. This structural compatibility allows Ti atoms to substitute up to 98 % of the Zr lattice sites without causing significant distortion (lattice strain < 1.2 %) [71–75].

Although the Zr-Ti solid solution phase in the U-MT5Z alloy gradually migrates toward the surface (simulating the cladding side) with elevating temperature, the commonly observed "Zr-depleted zones" at the cladding side in U-10Zr alloys [76] were not observed without a significant decrease in Zr concentration for the U-MT5Z. This difference suggests that the introduction of Ti may suppress the long-range migration of Zr, as further detailed in the following DFT calculation.

4.3. Effect of Ti-doping on the diffusion coefficient of U-MT5Z alloy

Before starting the calculations, we confirmed the accuracy of the model by comparing the XRD results with the lattice constants (Fig. S11). The formation energies (E_f) and post-relaxation atomic configurations of the two systems are first analyzed to provide a comprehensive understanding of the atomic diffusion behavior. Fig. 12a and b show the atomic configurations before relaxation. U-10Zr exhibits significant atomic displacements and distortions after relaxation. In contrast, the atomic arrangement in U-MT5Z remains relatively stable, and the local structure is well preserved, as indicated by the arrows in Fig. 12c and d. In addition, the RMSD for both systems was calculated, and the results show that U-MT5Z has an RMSD of 0.346 Å, which is clearly smaller than that of γ-(U, Zr) (0.518 Å). Further, the Zr atoms in U-10Zr tend to deviate from their original lattice positions after relaxation, whereas the relative positions of Zr in U-MT5Z remain almost unchanged, suggesting that the introduction of Ti effectively reduces local lattice distortions. Fig. 12e gives the formation energies of Zr vacancies in two systems. It is found that the Zr vacancy formation energy in U-MT5Z is higher than that in U-10Zr, which indicates that Zr vacancies are more difficult to form in U-MT5Z. A higher vacancy formation energy implies that Zr diffusion in U-MT5Z is suppressed since atomic diffusion typically involves the formation and migration of vacancies.

The Zr diffusion coefficient in U-10Zr is relatively higher across all crystallographic directions compared to U-MT5Z, with the most significant difference observed in the x-direction (4.78×10^{-6} vs. 4.61×10^{-7} m^2/s, approximately 10-fold) as shown in Fig. 12f. Moreover, U-MT5Z not only exhibits lower diffusion coefficients (decreasing by one order of

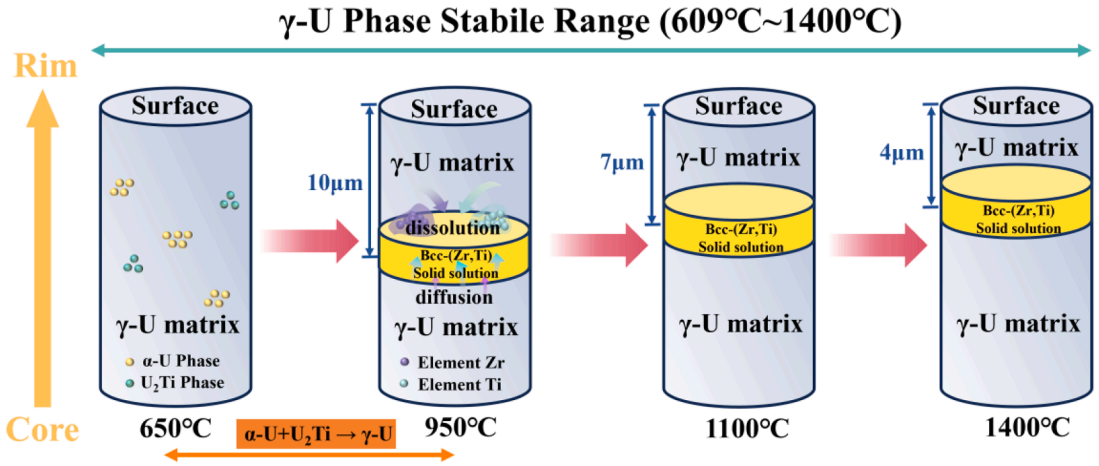

Fig. 11. Schematic illustration of the migration mechanism of the Zr-Ti solid solution. The bcc-(Zr, Ti) solid solution region progressively migrates from the interior toward the surface of the alloy with increasing temperature. This process is characterized by an upward shift and eventual enrichment of the solid solution near the surface, indicating a temperature-driven diffusion behavior.

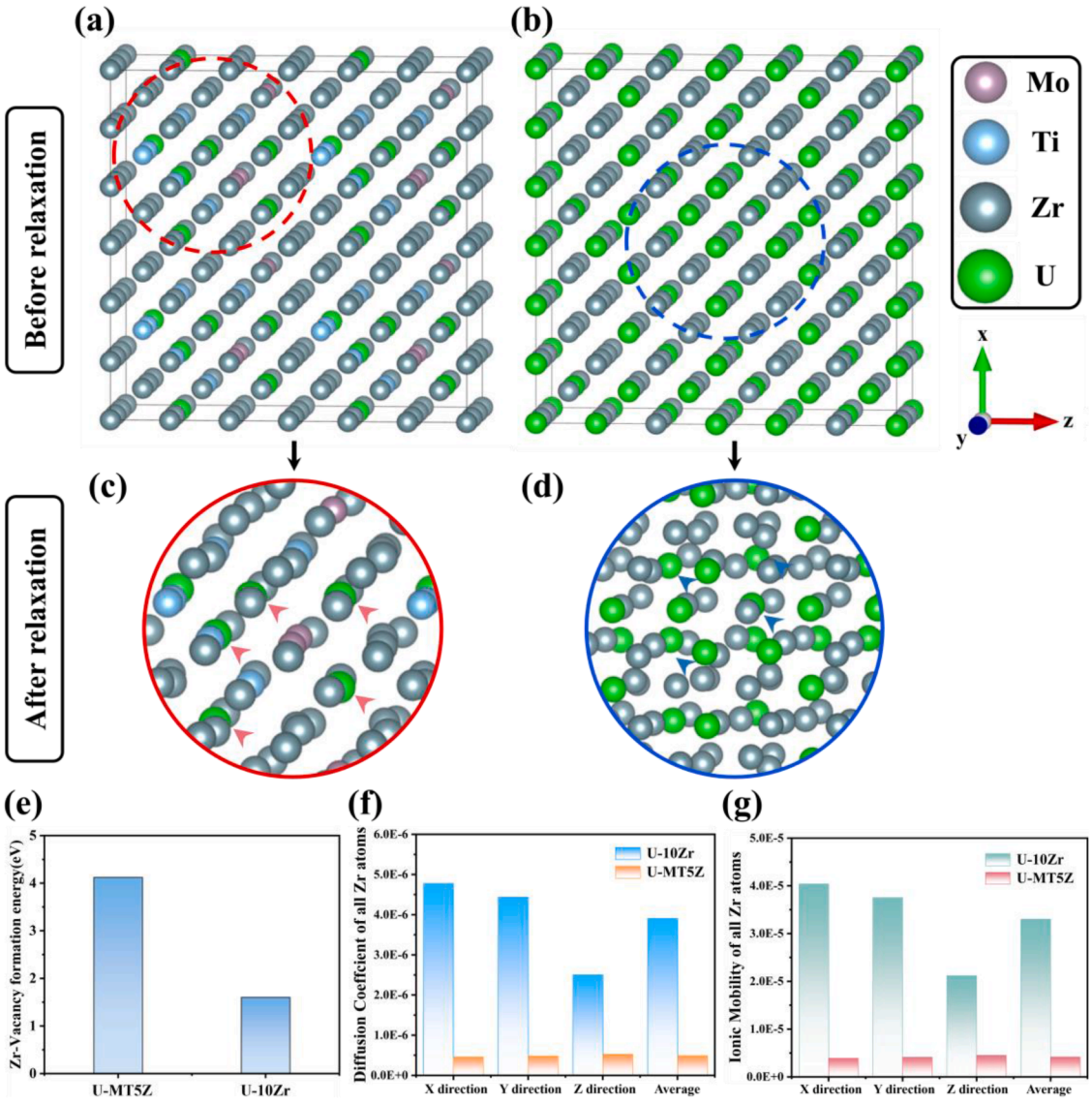

Fig. 12. First-principles-based comparison of the structural and diffusion properties between U-MT5Z and U-10Zr alloy models. (a) Initial atomic structures of U-MT5Z models, (b) Initial atomic structures of the U-10Zr models, (c)- (d) Spatial distribution of atoms in the two alloys after relaxation, (e)Formation energy of Zr vacancy in two alloys, (f)-(g) Diffusion coefficients and ionic mobilities of all Zr atoms in both models,.

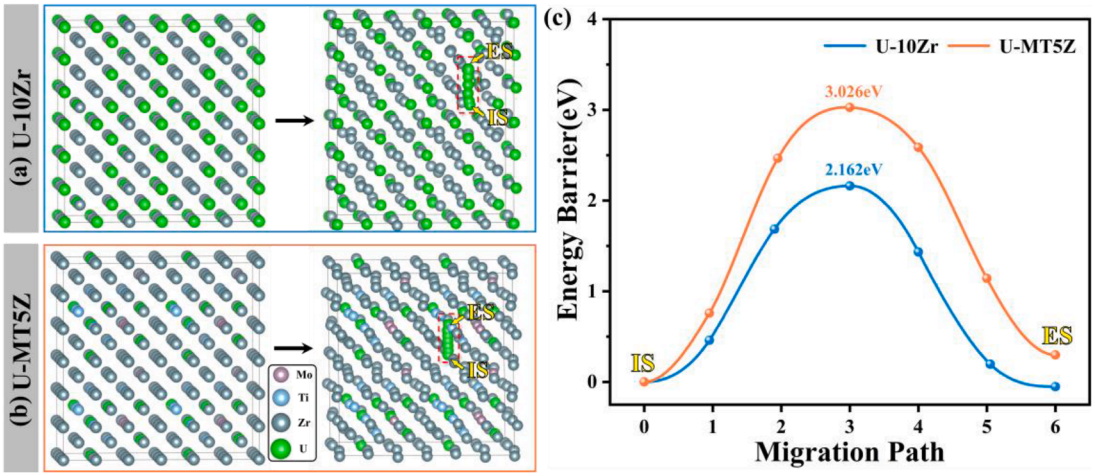

Fig. 13. Migration paths of Zr in (a)U-10Zr, (b)U-MT5Z, with their transition states shown in (c).

magnitude) but also demonstrates significantly weaker diffusion anisotropy compared to U-10Zr, suggesting that the incorporation of Ti effectively suppresses the directional migration of Zr atoms. The peak ionic mobility in the x-direction for U-10Zr (4.04×10^{-5} $m^2/V{\cdot}s$) is 10 times higher than that of U-MT5Z (3.89×10^{-6} $m^2/V{\cdot}s$), and a similar trend is observed in the average mobility, with a relative increase of 87.39 % ($\Delta\mu$) (Fig. 12g). Therefore, the incorporation of Ti effectively enhances the structural stability through delaying the diffusion of Zr atoms.

The migration paths of Zr in U-10Zr and U-MT5Z are shown in Fig. 13a and 13b, respectively, with the corresponding energy barriers to migration shown in Fig. 13c, where 0 and 1 represent the initial and final sites of the interstitial, respectively. The energy barrier for Zr migration in U-10Zr is the lowest at 2.162 eV, while it is 3.026 eV in U-MT5Z, suggesting that Zr in U-10Zr migrates more easily. Therefore, it is reasonable to conclude that Ti exerts a pinning effect on Zr migration in U-MT5Z. The presence of Ti alters the local lattice environment and forms strong chemical interactions with surrounding atoms, thereby increasing the migration barrier of Zr and suppressing its long-range migration.

The mechanism of Ti suppression of Zr migration primarily arises from the following aspects: firstly, Ti enhances the lattice stability of the alloy by forming a stable β phase (i.e., bcc-(Zr-Ti) solid solution) with Zr [77]. Meanwhile, the incorporation of Ti helps suppress lattice distortion and increases the vacancy formation energy of Zr, thereby reducing Zr atom diffusion. Second, the Zr's diffusion coefficient can further be reduced by Ti incorporation. In addition, the incorporation of Ti makes the diffusion of Zr atoms more isotropic, reducing Zr's directional nature and making Zr more homogeneously distributed. This indicates Ti doping reduces Zr migration in any specific direction and promotes a more uniform distribution of Zr within the alloy. Lastly, the first-principles calculations further confirm that Ti doping increases the migration energy barrier of Zr atoms, indicating that Ti stabilizes the alloy's phase structure thermodynamically and inhibits Zr diffusion and migration kinetically.

5. Conclusion

The current study systematically investigates the thermally driven behavior of the U-MT5Z alloy, focusing on the phase-composition evolution of the alloy matrix and Zr-containing precipitates, using a multiscale approach that combined DSC phase analysis, STEM-EDS characterization, and DFT simulation. The main results are summarized as follows:

1. The formation of U-MT5Z significantly lowers the α-U to γ-U phase transition temperature in U-based alloys (by approximately 9 %). It increases the upper thermodynamic stability regime of the γ-U phase (by approximately 13 %), which exhibits a broader thermal stability window for the γ-U phase compared to conventional U-10Zr alloys.
2. As the temperature increases, the U-MT5Z alloy gradually develops banded Zr-Ti solid solution phases, which eventually evolve into a trilayer structure. Meanwhile, the banded Zr-Ti solid-solution phase undergo directional axial migration from the center of the fuel to its surface.
3. Zr migration can be suppressed through the formation of Zr-Ti solid solution. DFT calculations further confirm that Ti effectively increases the migration barriers of Zr and significantly reduces its diffusion capability, thereby effectively suppressing Zr migration and enhancing the alloy's microstructural stability at elevated temperatures.

CRediT authorship contribution statement

Wangwei Ru: Writing – original draft, Data curation. **Kun Yang:** Writing – review & editing. **Weiqian Zhuo:** Writing – review & editing, Methodology. **Mingliang Kang:** Resources. **Danwen Qin:** Resources. **Yibo Wang:** Software, Methodology. **Xiaobin Tang:** Writing – review & editing.

Declaration of competing interest

The authors declare that they have no known competing financial interests or personal relationships that could have appeared to influence the work reported in this paper.

Acknowledgement

The authors would like to express appreciation for financial support from National Natural Science Foundation of China (No. 37244600); Natural Science Foundation of Jiangsu Province (BK20230898); this work is also supported by the Scientific Research Program for Young Talent of China National Nuclear Corporations (NPIC Z3022023006), and the Nuclear Technology R&D Program (Grant No. HJSYF2024(13)& HJSYF2025(08)); the microstructure characterization and phase identification are supported through Center for Microscopy and Analysis, Nanjing University of Aeronautics and Astronautics.

Supplementary materials

Supplementary material associated with this article can be found, in the online version, at doi:10.1016/j.actamat.2025.121875.

References

[1] D.C. Crawford, D.L. Porter, Applying U.S. metal fuel experience to new fuel designs for fast reactors, Prog. Nucl. Energy 171 (2024).
[2] L. Cai, F. Xu, F.G. Di Lemma, J.J. Giglio, M.T. Benson, D.J. Murray, C.A. Adkins, J. J. Kane, M. Xian, L. Capriotti, T. Yao, Understanding fission gas bubble distribution, lanthanide transportation, and thermal conductivity degradation in neutron-irradiated α-U using machine learning, Mater. Charact. 184 (2022).
[3] X. Liu, L. Capriotti, T. Yao, J.M. Harp, M.T. Benson, Y. Wang, F. Teng, L. He, Fuel-cladding chemical interaction of a prototype annular U-10Zr fuel with Fe-12Cr ferritic/martensitic HT-9 cladding, J. Nucl. Mater. 544 (2021).
[4] A Steady-State Analysis Of U-Pu-Zr Metallic Fuel Performance on Constituent Redistribution By Multiphysics Modeling.
[5] D. Salvato, X. Liu, D.J. Murray, K.M. Paaren, F. Xu, T. Pavlov, M.T. Benson, L. Capriotti, T. Yao, Transmission electron microscopy study of a high burnup U-10Zr metallic fuel, J. Nucl. Mater. 570 (2022).
[6] Y. Wang, C.B. Howard, F. Xu, D. Salvato, K.K. Bawane, D.J. Murray, D.M. Frazer, S. T. Anderson, T. Yao, S. Yeo, J.-H. Kim, B.-O. Lee, J.H. Kim, R.S. Fielding, L. Capriotti, Microstructural and micromechanical characterization of Cr diffusion barrier in ATR irradiated U-10Zr metallic fuel, J. Nucl. Mater. 599 (2024).
[7] G. Beausoleil, J. Zillinger, L. Hawkins, T. Yao, A.G. Weiss, X. Pu, N. Jerred, D. Kaoumi, Designing Nuclear Fuels with a Multi-Principal Element Alloying Approach, Nucl. Technol. 210 (3) (2024) 511–531.
[8] J.M. Harp, D.L. Porter, B.D. Miller, T.L. Trowbridge, W.J. Carmack, Scanning electron microscopy examination of a Fast Flux Test Facility irradiated U-10Zr fuel cross section clad with HT-9, J. Nucl. Mater. 494 (2017) 227–239.
[9] H. Okamoto, U-Zr (Uranium-Zirconium), J. Ph. Equilibria Diffus. 28 (5) (2007) 499–500.
[10] J.M. Harp, H.J. Chichester, L. Capriotti, Postirradiation examination results of several metallic fuel alloys and forms from low burnup AFC irradiations, J. Nucl. Mater. 509 (2018) 377–391.
[11] J. Kittel, B. Frost, J. Mustelier, K. Bagley, G. Crittenden, J. Van Dievoet, History of fast reactor fuel development, J. Nucl. Mater. 204 (1993) 1–13.
[12] R. Mariani, D. Porter, J. Kennedy, S. Hayes, V. Blackwood, Z. Jones, D. Olson, B. Mishra, New fuel alloys seeking optimal solidus and phase behavior for high burnup and TRU burning, Fast Reactors and Related Fuel Cycles: safe Technologies and Sustainable Scenarios (FR13). COMPANION CD-ROM, in: Proceedings of an International Conference, 2015, p. 7. -7.
[13] R.D. Mariani, D.L. Porter, S.L. Hayes, J.R. Kennedy, Metallic fuels: the EBR-II legacy and recent advances, Procedia Chem. 7 (2012) 513–520.
[14] J.M. Harp, L. Capriotti, F. Cappia, Postirradiation Examination of Recently Irradiated Metallic Fuel Concepts, Idaho National Lab.(INL), Idaho Falls, ID (United States), 2018.
[15] V.S. Blackwood, As-cast Uranium-Molybdenum Based Metallic Fuel Candidates and the Effects of Carbon Addition, 2014.
[16] C.T. Howard, The behavior of palladium as a getter for lanthanide fission products in U-Mo-Ti-Zr fast reactor fuels, Colo. Sch. Mines (2017).
[17] W. Zhuo, Y. Xie, M.T. Benson, J. Ge, R.D. Mariani, J. Zhang, XRD and SEM/EDS characterization of two quaternary fuel alloys (U-2.5 Mo-2.5 Ti-5.0 Zr and U-1.5 Mo-1.5 Ti-7.0 Zr in wt.%) for fast reactors, Mater. Charact. 170 (2020) 110696.

[18] W. Zhuo, H. Wu, Y. Xie, M.T. Benson, J. Zhang, Solid-state phase transitions of two quaternary metallic fuel alloys (U-2.5 Mo-2.5 Ti-5.0 Zr and U-1.5 Mo-1.5 Ti-7.0 Zr in wt.%), J. Nucl. Mater. 555 (2021) 153134.
[19] V. Blackwood, Z. Jones, D. Olson, B. Mishra, R. Mariani, D. Porter, J. Kennedy, S. Hayes, New Fuel Alloys Seeking Optimal Solidus and Phase Behavior For High Burnup and TRU Burning, 2013.
[20] I.A. Ditenberg, I.V. Smirnov, M.A. Korchagin, K.V. Grinyaev, V.V. Melnikov, Y. P. Pinzhin, A.I. Gavrilov, M.A. Esikov, V.I. Mali, D.V. Dudina, Structure and phase composition of a W-Ta-Mo-Nb-V-Cr-Zr-Ti alloy obtained by ball milling and spark plasma sintering, Entropy 22 (2) (2020) 143.
[21] J. Buckley, D. Goddard, T. Abram, Studies on the spark plasma sintering of U3Si2: processing parameters and interactions, J. Nucl. Mater. 544 (2021) 152655.
[22] K. Yang, E. Kardoulaki, D. Zhao, A. Broussard, K. Metzger, J.T. White, M.R. Sivack, K.J. Mcclellan, E.J. Lahoda, J. Lian, Uranium nitride (UN) pellets with controllable microstructure and phase–fabrication by spark plasma sintering and their thermal-mechanical and oxidation properties, J. Nucl. Mater. 557 (2021) 153272.
[23] R. Harrison, J. Morgan, J. Buckley, T. Abram, D. Goddard, N. Barron, Spark plasma sintering of (U, Ce) O2 as a MOx nuclear fuel surrogate, J. Nucl. Mater. 557 (2021) 153302.
[24] G. Kresse, J. Furthmüller, Efficiency of ab-initio total energy calculations for metals and semiconductors using a plane-wave basis set, Comput. Mater. Sci. 6 (1) (1996) 15–50.
[25] G. Kresse, J. Hafner, Ab initio molecular dynamics for liquid metals, Phys. Rev. B 47 (1) (1993) 558.
[26] B. Beeler, D. Andersson, C. Jiang, Y. Zhang, Ab initio molecular dynamics investigation of point defects in γ-U, J. Nucl. Mater. 545 (2021) 152714.
[27] Y. Park, N. Eriksson, R. Newell, D. Keiser, Y. Sohn, Phase decomposition of γ-U (bcc) in U-10 wt% Mo fuel alloy during hot isostatic pressing of monolithic fuel plate, J. Nucl. Mater. 480 (2016) 271–280.
[28] H. Okamoto, M. Schlesinger, E. Mueller, Mo (Molybdenum) Binary Alloy Phase Diagrams, Alloy Ph. Diagr. 3 (2016) 496.
[29] G. Park, B. Beeler, M.A. Okuniewski, An atomistic study of defect energetics and diffusion with respect to composition and temperature in γU and γU-Mo alloys, J. Nucl. Mater. 552 (2021) 152970.
[30] J.P. Perdew, K. Burke, M. Ernzerhof, Generalized gradient approximation made simple, Phys. Rev. Lett. 77 (18) (1996) 3865.
[31] A. Aly, B. Beeler, M. Avramova, Ab initio molecular dynamics investigation of γ-(U, Zr) structural and thermal properties as a function of temperature and composition, J. Nucl. Mater. 561 (2022) 153523.
[32] H.J. Monkhorst, J.D. Pack, Special points for Brillouin-zone integrations, Phys. Rev. B 13 (12) (1976) 5188.
[33] M. Cococcioni, S. De Gironcoli, Linear response approach to the calculation of the effective interaction parameters in the LDA+ U method, Phys. Rev. B—Condens. Matter Mater. Phys. 71 (3) (2005) 035105.
[34] N. Wang, J. Tian, T. Jiang, Y. Yang, S. Hu, S. Peng, L. Yan, Energetics of gaseous and volatile fission products in molten U–10Zr alloy: a density functional theory study, J. Nucl. Mater. 466 (2015) 583–587.
[35] N. Wang, T. Jiang, Y. Yang, J. Tian, S. Hu, S. Peng, L. Yan, Embedded atom model for the liquid U–10Zr alloy based on density functional theory calculations, RSC Adv. 5 (76) (2015) 61495–61501.
[36] K. Momma, F. Izumi, VESTA 3 for three-dimensional visualization of crystal, volumetric and morphology data, Appl. Crystallogr. 44 (6) (2011) 1272–1276.
[37] S.M. Zamzamian, A. Zolfaghari, Z. Kowsar, Molecular dynamics investigation of xenon, uranium, and oxygen diffusion in UO2 nuclear fuel, Comput. Mater. Sci. 211 (2022) 111553.
[38] M. Kovalenko, A.Y. Kupryazhkin, Mechanisms of exchange and anion frenkel diffusion in uranium dioxide: molecular dynamics study, J. Nucl. Mater. 522 (2019) 255–264.
[39] C.Jose Palathinkal, J.R. Lukes, Local Diffusion Coefficients in Spherically Symmetric Systems Using the Smoluchowski Equation and Molecular Dynamics, J. Phys. Chem. B 129 (11) (2025) 3073–3082.
[40] E. Vathonne, D.A. Andersson, M. Freyss, R. Perriot, M.W. Cooper, C.R. Stanek, M. Bertolus, Determination of krypton diffusion coefficients in uranium dioxide using atomic scale calculations, Inorg. Chem. 56 (1) (2017) 125–137.
[41] C. Matthews, R. Perriot, M.W.D. Cooper, C.R. Stanek, D.A. Andersson, Cluster dynamics simulation of xenon diffusion during irradiation in UO2, J. Nucl. Mater. 540 (2020) 152326.
[42] A. Goyal, S.R. Phillpot, G. Subramanian, D.A. Andersson, C.R. Stanek, B. P. Uberuaga, Impact of homogeneous strain on uranium vacancy diffusion in uranium dioxide, Phys. Rev. B 91 (9) (2015) 094103.
[43] L. Yang, N. Kaltsoyannis, Diffusion of krypton and xenon in uranium mononitride; a Density Functional Theory Study, J. Nucl. Mater. 566 (2022) 153803.
[44] W. Zhuo, Development of Metallic Fuel Additives and Alloys for Sodium-cooled Fast Reactors, 2022.
[45] J. Speer, D. Edmonds, An investigation of the γ→ α martensitic transformation in uranium alloys, Acta Metall. 36 (4) (1988) 1015–1033.
[46] T.H. Chang, M. Adachi, M. Ueda, M. Ikeda, Mechanical Property and Heat Treatment Behaviour of Ti-Zr-Fe Alloys, Mater. Sci. Forum Trans. Tech. Publ. (2021) 1479–1484.
[47] Y. Jeong, C.N. Tomé, Thermal ratcheting of uranium simulated with a thermo-elasto-visco-plastic self-consistent polycrystal model, J. Nucl. Mater. 597 (2024) 155159.
[48] K.L. Murty, I. Charit, An Introduction to Nuclear materials: Fundamentals and Applications, John Wiley & Sons, 2013.
[49] D. Jain, J. Nuwad, V. Sudarsan, A. Tyagi, Effect of structural phase transitions on high temperature thermal conductivity of nuclear-grade uranium, J. Alloys. Compd. 831 (2020) 154706.
[50] U (Uranium) Binary Alloy Phase Diagrams, in: H. Okamoto, M.E. Schlesinger, E. M. Mueller (Eds.), Alloy Phase Diagrams, ASM International, 2016, p. 0.
[51] R. Rakesh, A. Jain, V. Sinha, R. Tewari, Gamma Phase Stability in U–Mo Alloys, Trans. Indian Inst. Met. 76 (2023) 1997–2007.
[52] B. Hatt, The orientation relationship between the gamma and alpha structures in uranium-zirconium alloys, J. Nucl. Mater. 19 (1966) 133–141.
[53] M. Aizenshtein, D. Hamawi, Structural Insights in the β to α Phase Transformation of the U–1 wt.% Ga–0.2 wt.% Fe Alloy, Metallogr. Microstruct. Anal. 3 (2014) 454–459.
[54] W. Chen, X. Bai, Development of Thermal Conductivity Models for U-Zr and UPu Alloys, 2018.
[55] M. Poschmann, M.H. Piro, T.M. Besmann, K.T. Clarno, S. Simunovic, Thermochemically-informed mass transport model for interdiffusion of U and Zr in irradiated U-Pu-Zr fuel with fission products, J. Nucl. Mater. 554 (2021) 153089.
[56] W. Chen, X.-M. Bai, Temperature and composition dependent thermal conductivity model for U-Zr alloys, J. Nucl. Mater. 507 (2018) 360–370.
[57] C. Wen, W. Liu, D. Yun, Z. Qian, A phase-field model with irradiation-enhanced diffusion for constituent redistribution in U-10wt% Zr metallic fuels, Front. Mater. 9 (2022) 950785.
[58] Y.S. Kim, G. Hofman, S. Hayes, Y. Sohn, Constituent redistribution in U–Pu–Zr fuel during irradiation, J. Nucl. Mater. 327 (1) (2004) 27–36.
[59] A. Aitkaliyeva, Recent trends in metallic fast reactor fuels research, J. Nucl. Mater. 558 (2022) 153377.
[60] K.E. Wright, L. Lecrivain, C. Pincock, M. Coleman, P. Wiscaver, B. Barker, L.G. R. Albuquerque, L. Capriotti, A. Aitkaliyeva, Exploring constituent redistribution in irradiated U-19Pu-14Zr fuel via electron probe microanalysis, J. Nucl. Mater. 603 (2025) 155411.
[61] T. Rahn, B.D. Miller, L. Capriotti, A. Aitkaliyeva, TEM-based phase characterization of U–19Pu–10Zr irradiated in ATR, MRS Bull. 48 (4) (2023) 351–360.
[62] X. Chen, Z. Xie, X. Mao, S. Ding, Modeling of Zirconium Atom Redistribution and Phase Transformation Coupling Behaviors in U-10Zr-Based Helical Cruciform Fuel Rods under Irradiation, Metals 14 (7) (2024) 745.
[63] W. Williams, D. Wachs, M. Okuniewski, S. Van Den Berghe, Assessment of swelling and constituent redistribution in uranium-zirconium fuel using phenomena identification and ranking tables (PIRT), Ann. Nucl. Energy 136 (2020) 107016.
[64] J.J. Cox, E.R. Homer, V. Tikare, M. Kurata, Simulated microstructural and compositional evolution of U-Pu-Zr alloys using the Potts-phase field modeling technique, Metall. Mater. Trans. A 49 (2018) 6457–6468.
[65] M. Aizenshtein, E. Brosh, Z. Ungarish, S. Levi, M. Tubul, D. Fadel, E. Greenberg, S. Hayun, High entropy uranium-based alloys: thermodynamics, characterization and mechanical properties, J. Nucl. Mater. 558 (2022) 153378.
[66] G. Hofman, S. Hayes, M. Petri, Temperature gradient driven constituent redistribution in U Zr alloys, J. Nucl. Mater. 227 (3) (1996) 277–286.
[67] Z. Qu, Z. Liu, Y. Zhao, G. Shang, W. Feng, Thermodynamic Assessment of the U-Ti-Zr System and Atomic Mobility of Its bcc Phase, J. Ph. Equilibria Diffus. (2025) 1–10.
[68] H. Saller, F. Rough, A. Bauer, J. Doig, Constitution of delta-phase alloys of the system U-Zr-Ti, J. Met. 9 (1957).
[69] T.J. Lee, T. Ueno, N. Nomura, N. Wakabayashi, T. Hanawa, Titanium-Zirconium Binary Alloy as Dental Implant Material: analysis of the Influence of Compositional Change on Mechanical Properties and In Vitro Biologic Response, Int. J. Oral Maxillofac. Implants 31 (3) (2016).
[70] E.J. Mittemeijer, Fundamentals of Materials Science, Springer, 2010.
[71] L. Aissani, M. Fellah, C. Nouveau, M. Abdul Samad, A. Montagne, A. Iost, Structural and mechanical properties of Cr–Zr–N coatings with different Zr content, Surf. Eng. 36 (1) (2020) 69–77.
[72] J. Zhang, C. Wang, N. Shareef, Microstructure and properties of Ti-Zr-Mo alloys fabricated by laser directed energy deposition, Materials 16 (3) (2023) 1054.
[73] R. Janknecht, N. Koutná, K. Weiss, E. Ntemou, S. Kolozsvári, P.H. Mayrhofer, R. Hahn, Strategic lattice manipulation in transition metal nitrides for improved solubility, Acta Mater. 283 (2025) 120514.
[74] Y.A. Mityushova, A. Gibadullina, E. Zhilina, A. Russkikh, S. Krasikov, Thermodynamic estimation of the formation of a high-entropy Al–Nb–Ti–V–Zr alloy, Russ. Metall. (Met.) 2021 (2021) 187–191.
[75] L. Li, Q. Fang, J. Li, B. Liu, Y. Liu, P.K. Liaw, Lattice-distortion dependent yield strength in high entropy alloys, Mater. Sci. Eng.: A 784 (2020) 139323.
[76] X. Liu, L. Capriotti, T. Yao, J.M. Harp, M.T. Benson, Y. Wang, F. Teng, L. He, Fuel-cladding chemical interaction of a prototype annular U-10Zr fuel with Fe-12Cr ferritic/martensitic HT-9 cladding, J. Nucl. Mater. 544 (2021) 152588.
[77] K.H. Kumar, P. Wollants, L. Delacy, Thermodynamic assessment of the Ti Zr system and calculation of the Nb Ti Zr phase diagram, J. Alloys Compd. 206 (1) (1994) 121–127.